Medical Image Analysis 79 (2022) 102446

Contents lists available at ScienceDirect

Medical Image Analysis

journal homepage: www.elsevier.com/locate/media

Characterizing the propagation pathway of neuropathological events of Alzheimer's disease using harmonic wavelet analysis

Jiazhou Chen[a], Hongmin Cai[a], Defu Yang[b], Martin Styner[c,d,f], Guorong Wu[c,d,e,f,*], Alzheimer's-Disease-Neuroimaging-Initiative-(ADNI)[a]

[a] School of Computer Science and Engineering, South China University of Technology, Guangzhou, China
[b] Intelligent Information Processing Laboratory, Hangzhou Dianzi University, Hangzhou, China
[c] Department of Psychiatry, University of North Carolina at Chapel Hill, United States
[d] Department of Computer Science, University of North Carolina at Chapel Hill, United States
[e] Department of Statistics and Operations Research, University of North Carolina at Chapel Hill, United States
[f] Carolina Institute for Developmental Disabilities, University of North Carolina at Chapel Hill, United States

ARTICLE INFO

Article history:
Received 15 September 2021
Revised 7 March 2022
Accepted 1 April 2022
Available online 6 April 2022

Keywords:
Brain network
Harmonic wavelets
Manifold optimization
Alzheimer's disease

ABSTRACT

Empirical imaging biomarkers such as the level of the regional pathological burden are widely used to measure the risk of developing neurodegenerative diseases such as Alzheimer's disease (AD). However, ample evidence shows that the brain network (wirings of white matter fibers) plays a vital role in the progression of AD, where neuropathological burdens often propagate across the brain network in a prion-like manner. In this context, characterizing the spreading pathway of AD-related neuropathological events sheds new light on understanding the heterogeneity of pathophysiological mechanisms in AD. In this work, we propose a manifold-based harmonic network analysis approach to explore a novel imaging biomarker in the form of the AD propagation pattern, which eventually allows us to identify the AD-related spreading pathways of neuropathological events throughout the brain. The backbone of this new imaging biomarker is a set of region-adaptive harmonic wavelets that represent the common network topology across individuals. We conceptualize that the individual's brain network and its associated pathology pattern form a unique system, which vibrates as do all natural objects in the universe. Thus, we can computationally excite such a brain system using selected harmonic wavelets that match the system's resonance frequency, where the resulting oscillatory wave manifests the system-level propagation pattern of neuropathological events across the brain network. We evaluate the statistical power of our harmonic network analysis approach on large-scale neuroimaging data from ADNI. Compared with the other empirical biomarkers, our harmonic wavelets not only yield a new imaging biomarker to potentially predict the cognitive decline in the early stage but also offer a new window to capture the *in-vivo* spreading pathways of neuropathological burden with a rigorous mathematics insight.

1. Introduction

Alzheimer's disease (AD) is the most common neurodegenerative disease often characterized by memory upset, behavioral and cognitive decline as aging (Blennow et al., 2006). AD is a progressive disease such that it starts from mild cognitive impairment (MCI) (Reisberg et al., 2008; Vemuri et al., 2009) and gradually spreads throughout the brain until the damage reaches the occipital lobe in individuals that survive through to severe stages of AD. Due to the overlapping nature with the typical aging effect, reliable AD biomarker becomes critical in staging the neurodegenerative process and predicting the risk of developing AD before the onset of clinical symptoms.

In the National Institute of Aging and Alzheimer's Association (NIA-AA) research framework (Jack et al., 2018), AD biomarkers are grouped into amyloid β (Aβ) deposition (Bloom, 2014), pathologic tau (Braak and Del Tredici, 2018), and neurodegeneration (Devanand et al., 2010) (A-T-N). Although progressive neuron loss is a hallmark of AD (Morrison and Hof, 1997; Schaeffer et al., 2011; Serran-Pozo et al., 2011), converging evidence shows that AD-related neurological impairment may reflect dysfunction rather than loss of neurons (Matthews et al., 2012; Palop et al., 2006; Pievani et al., 2014). In this regard, AD can be understood as a disconnection syndrome where the large-scale brain network is progressively disrupted by neuropathological processes

* Corresponding author.
E-mail address: grwu@med.unc.edu (G. Wu).

https://doi.org/10.1016/j.media.2022.102446
1361-8415/

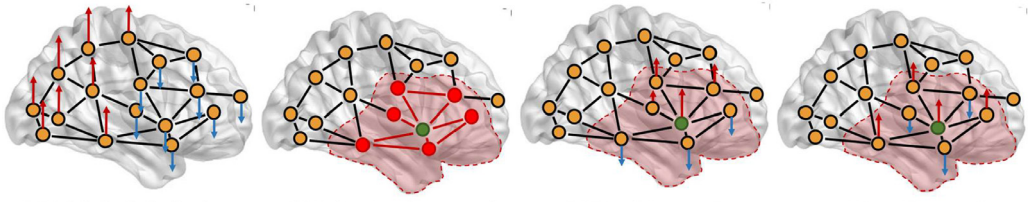

Fig. 1. (a) The global nature of whole-brain harmonic waves precludes the identification of local propagation patterns that are presented within the associated subnetwork. Since we derive the region-adaptive harmonic wavelets within the associated subnetwork centered at each node (b), our harmonic wavelets (c-d) depict the local network oscillation, which allows us to capture the spatial-spectrum harmonic patterns in brain network inference.

(Pievani et al., 2014). Recently, the research focus has been shifted to characterize the propagation patterns of A-T-N biomarkers throughout the brain (Raj et al., 2012, 2015; Vogel et al., 2020, 2021). For example, an epidemic spreading model is employed in Vogel et al. (2020) to simulate tau spread, which can explain up to 70% variance in the overall spatial pattern of tau among 312 individuals along the Alzheimer's disease continuum.

Recent developments in diffusion-weighted MRI and network neuroscience allow us to characterize the white matter pathway capturing how gray matter regions are connected in the context of the large-scale brain network. The network degeneration hypothesis – significant changes might occur in the topological properties of structural brain network as AD progresses – is supported by many neuroimaging studies (Araque Caballero et al., 2018; Filippi et al., 2017). In addition, convergent evidence shows that the presence of AD pathology burden exhibits a unique spatial pattern that is highly correlated with the region-to-region connections in the network (Braak and Braak, 1996; Sepulcre et al., 2018; Wu et al., 2016). All pieces of evidence put the spotlight on the investigation of the spreading pathway of A-T-N biomarkers in the context of region-to-region connectivity.

In our previous work (Chen et al., 2020a, 2020b), we presented a network harmonic analysis approach to characterize the network alterations in the graph spectrum domain. Specifically, we assume the spreading of the neuropathological burden follows the wires of white matter fibers. Since the neuropathological events running on the brain network are steered by the topology of these wirings, we regard the regional level of neuropathological burden as the graph signal, instead of the data array, where the element-wise relationship in the graph signal is characterized by the connectivity in the network. By doing so, we use the eigenvectors (called harmonic waves) of the underlying graph Laplacian as the basis function to represent the observed instance of the graph signal. Furthermore, we proposed a manifold-based approach to unify the eigenvectors from individual brain networks into a set of common harmonic waves, which provides a reference to compare and quantify individual differences in the graph spectrum domain.

Harmonic waves provide building blocks to form biological patterns (e.g., the animal coats in morphogenesis) and physical patterns in acoustics and quantum mechanics. In Chen et al. (2020a), we have applied the principles of these harmonic waves into the anatomy of the human brain, which emerges a new network analysis approach using network-specific harmonic waves. The common harmonic waves constitute a new neurobiological basis for understanding disease progression, where each harmonic wave exhibits a unique propagation pattern of neuro-pathological burdens spreading across brain networks. Although promising results have been demonstrated in identifying AD-related harmonic alterations, the global nature of harmonic waves (Fig. 1(a)) limits their application in characterizing the local propagation of neuropathological burden across the associated subnetworks in the brain.

To overcome this limitation, we propose a novel manifold harmonic localization approach to extend our whole-brain harmonic waves to region-adaptive harmonic wavelets (Fig. 1(c-d)), which are localized at each brain region (Fig. 1(b)). Specifically, we optimize the harmonic wavelets on top of the global harmonic waves such that the learned harmonic wavelets are complementary (orthogonal) to the existing whole-brain harmonic bases. Since the harmonic wavelets opt to capture the local network topology, the region adaptive characteristics allow us to investigate the spreading pathway of AD-related neuropathological events. Furthermore, the oscillation pattern presented in each harmonic wavelet (in the spectrum domain) and the localized sub-network (in the spatial domain) offer a new window to investigate the spatial-spectrum alteration of neuropathological events across the brain network. As a result, the localized harmonic-like pattern captured by our harmonic wavelet analysis is more attractive than the current neuroimaging biomarkers, which merely focus on the concentration level of neuropathological burden at each region.

We have evaluated the statistical power of our method on synthetic data and neuroimaging data from the ADNI database. Compared with other popular empirical biomarkers, our proposed method achieves higher discrimination power for disentangling CN (cognitively normal), EMCI (early-stage mild cognitive impairment), and LMCI (late-state mild cognitive impairment) comparison. Moreover, we have identified a set of brain regions (called distributors) that are not only actively involved in the distribution of pathological proteins (such as amyloid and tau) but also lead to cognitive decline. Since these identified distributor regions receive and pass on the neuropathological burdens faster than the other brain regions, the observed concentration levels might not be as high as the high-risk regions in the PET (positron emission tomography) scans that are often reported in the literature. However, our harmonic wavelet analysis results imply that special attention should be paid to the distributor regions in predicting the risk of developing AD, mainly due to the progressive nature of AD.

1.1. Relevant work

Tremendous efforts have been made to explore the geometry patterns manifested in neuroimages. For example, the convoluted foldings along the brain cortical surface demand the manifold-based algebra to model the diffusion process across the sulcus and gyrus. Conventional Euclidian operations often yield biologically unreasonable effects due to the gross simplification that data resides on a flat space, which is partially responsible for the lack of reproducible findings in cortex analysis. To address this challenge, the spectral graph wavelet transform (Tan and Qiu, 2015) has been developed to model the shape geometry of the cortical surface mesh, where the construction of these wavelets is governed by the Laplacian-Beltrami operator of the underlying surface mesh. Recently, Huang et al. (2020) proposed an efficient multi-

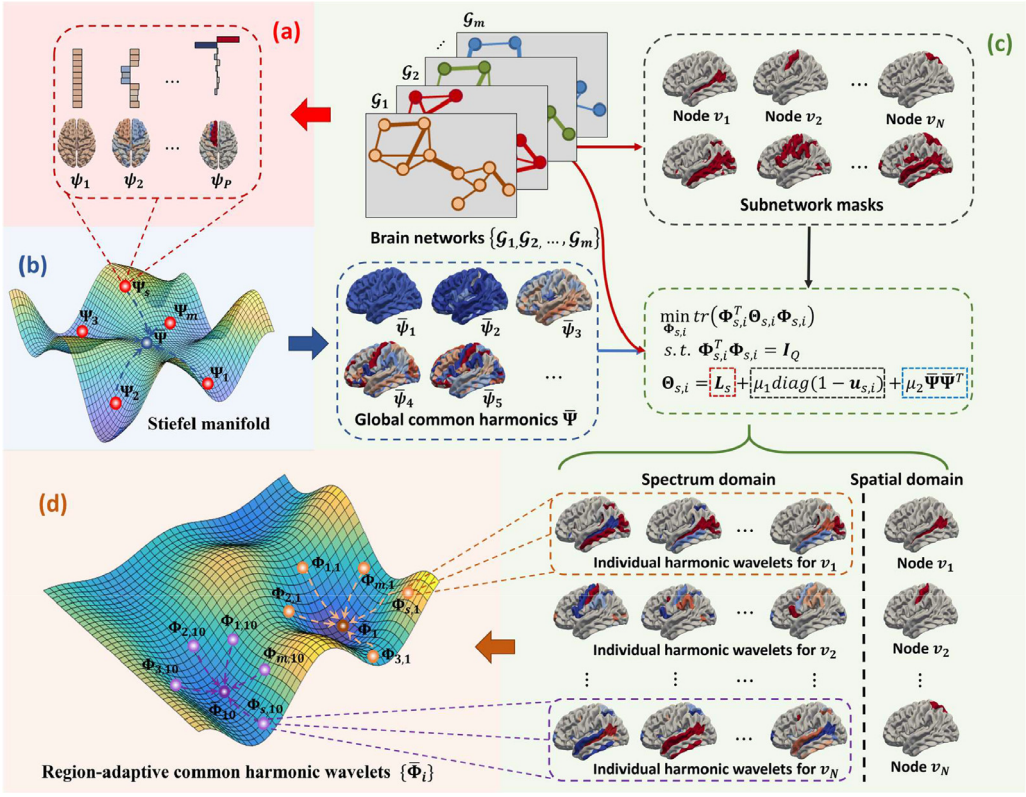

Fig. 2. Illustration of the workflow. (a) Individual-based harmonic waves $\mathbf{\Psi}_s$ is calculated by eigen-decomposition of graph Laplacian matrix of its underlying brain network $\mathcal{G}_s$. (b) The global common harmonic waves $\bar{\mathbf{\Psi}}$ is learned by iteratively adjusting each $\mathbf{\Psi}_s$ and updating the manifold center on the Stiefel manifold. (c) The region-based individual harmonic wavelets $\mathbf{\Phi}_{s,i}$ of node v_i in brain network $\mathcal{G}_s$ is estimated by minimizing three energy terms, including topology preservation in red, subnetwork localization penalty in black, and redundancy removal in blue. (d) Finally, the region-based common harmonic wavelets $\bar{\mathbf{\Phi}}_i$ is obtained by learning the Fréchet mean from a population of $\{\mathbf{\Phi}_{s,i} | s = 1, \cdots, m\}$ for node v_i on the Stiefel manifold.

scale approach to model the brain sulcal and gyral growth patterns in brain development. Enlighted by these pioneer works, we put the spotlight on the graph Laplacian of brain network and present a manifold-based harmonic wavelet analysis framework to characterize the propagation events of neuropathologies throughout the brain. It is worth noting that current state-of-the-art methods solve the wavelet base functions on an individual basis. However, our work aims to estimate the common harmonic wavelets (at the population level) that can provide a standardized measurement of pathology propagation across subjects. Thus, the harmonic wavelets in our work are the approximation to the graph wavelets constructed in Huang et al. (2020), Kim et al. (2015), Tan and Qiu (2015).

In this paper, we develop a set of manifold-based algebra and optimization methods that are tailored to the Eigen-system of the brain network. Compared to current biomarker studies, our harmonic wavelets analysis framework respects the geometry of network data and yields more putative harmonic-like biomarkers with great mathematics insight. On top of this, our contributions to the neuroimaging and neuroscience field have two folds. (1) We propose a novel harmonic-like biomarker to characterize the propagation patterns underlying the disease progression, which allows us to advance our underpinning of the pathophysiological mechanism of neurodegenerative diseases and diagnose disease in the early stage. We demonstrate that our proposed method not only discovers the spreading pathways of neuropathological events but also provides a new imaging biomarker with higher discrimination power for predicting the early stage of AD than other empirical biomarkers. (2) As a proof-of-concept approach, the spatial-spectrum analysis framework offers a new window to capture the propagation pathway of neuropathological events throughout the brain. Furthermore, we demonstrate the potential application of our harmonic wavelet analysis in identifying the critical brain regions that are actively involved in the spreading of neuropathological burdens, which might provide a new clue to understanding neurodegenerative diseases.

2. Method

Fig. 2 outlines our learning-based approach of extending from harmonic waves to harmonic wavelets. In general, our method consists of four steps. (1) *Calculate individual harmonic waves.* It is straightforward to calculate each harmonic wave by the eigen-decomposition of graph Laplacian matrix of its underlying brain network, as shown in Fig. 2(a). (2) *Estimating global common harmonic waves.* As demonstrated in Fig. 2(b), we deploy our manifold-based optimization method (Chen et al., 2020a) to obtain the common harmonic waves across the individual harmonic waves in step (1), which acts as the reference to infer harmonic wavelets at each brain region. (3) *Optimizing region-adaptive harmonic wavelets within each subject.* We present an optimization approach to estimate the harmonic wavelets at each brain region (Fig. 2(c)), which is required to capture the local network topology centered at the underlying region and maintain orthogonality to global common harmonic waves (in step 2). (4) *Inferring common harmonic wavelets.* Given a set of region-adaptive harmonic wavelets, we identify the common harmonic wavelets region by region, which is essentially the Fréchet mean on the manifold, as illustrated in Fig. 2(d). The output is the localized common harmonic wavelets associated with each node in the brain network. The wavelets can be used to explain and characterize the local propagation pattern of neuropathological events across brain net-

works. In the following, we first present the objective functions used in the above four steps from Section 2.1 to Section 2.4. Then we give the detail of optimization in Section 2.5. We demonstrate the potential applications of harmonic wavelets in Section 2.6.

2.1. Brain network and harmonic waves

Mathematically, each brain network constructed through MRI and DTI neuroimages can be encoded as a graph $\mathcal{G} = (V, \mathcal{E}, \boldsymbol{W})$, with node set $V = \{v_i | i \in 1, \cdots, N\}$ from N brain regions and edge set $\mathcal{E} = \{e_{ij} | (v_i, v_j) \in V \times V\}$ representing all possible interactions between nodes. Let matrix $\boldsymbol{W} = [w_{ij}\ ]_{N\times N} \in \mathbb{R}^{N\times N}$ be the symmetric adjacency matrix with non-negative weights w_{ij} between the network node v_i and v_j. Then, we compute the symmetric graph Laplacian matrix $\boldsymbol{L}$ on each underlying graph as:

$$\boldsymbol{L} = \boldsymbol{D} - \boldsymbol{W}. \tag{1}$$

where the i^{th} diagonal element $\boldsymbol{D}(i,i) = \sum_{j=1}^{N} w_{ij}$ for the diagonal matrix $\boldsymbol{D}$ can be regarded as the degree matrix of the graph. Each diagonal element is equal to the total connectivity degree of the underlying node.

As stated in Atasoy et al. (2016), we calculate a set of individual harmonic waves by solving the following eigenvalue problem:

$$\min_{\boldsymbol{\Psi}\in\mathbb{R}^{N\times P}} tr\left(\boldsymbol{\Psi}^{\mathrm{T}}\boldsymbol{L}\boldsymbol{\Psi}\right), \quad s.t.\ \ \boldsymbol{\Psi}^{\mathrm{T}}\boldsymbol{\Psi} = \boldsymbol{I}_P \tag{2}$$

where $tr(\cdot)$ is the trace operator and $\boldsymbol{I}_P$ denotes the $P \times P$ identity matrix. The deterministic solution $\boldsymbol{\Psi}$ of the optimization problem in Eq. (2) is a set of eigenvectors of the Laplacian matrix $\boldsymbol{L}$. It is worth noting that the eigenvectors $\boldsymbol{\Psi}$ are sorted column by column in increasing order of eigenvalues $\{\lambda_p | p = 1, \cdots, P, \lambda_1 \le \lambda_2 \le \cdots \le \lambda_P\}$ (Chavel, 1984), indicating the harmonic wave exhibits faster oscillation patterns across the brain network as the eigenvalue increases. Since the harmonic waves associated with the high frequency (larger eigenvalues) are often sensitive to possible noise, we only consider the first P ($P < N$) harmonic waves. Given that each individual harmonic set $\boldsymbol{\Psi}$ is an $N \times P$ orthogonal matrix, it is reasonable to consider $\boldsymbol{\Psi}$ of the individual brain network as an instance drawn from Stiefel manifold (Chikuse, 2012).

2.2. Estimation of global common harmonic waves

Given m brain networks $\mathcal{G}_s (s = 1, \cdots, m)$, the individual harmonic waves $\boldsymbol{\Psi}_s$ (an orthogonal matrix) thus can be obtained by optimizing the objective function in Eq. (2). We are now interested in estimating the mean $\bar{\boldsymbol{\Psi}}$ of all individual harmonic waves $\{\boldsymbol{\Psi}_s | s = 1, \cdots, m\}$. It is served as a brain network unbiased reference, and is called the global common harmonic waves. It is also an orthogonal matrix. Mathematically, we require the global common harmonic waves $\bar{\boldsymbol{\Psi}}$ to be close to the manifold center with the shortest geodesic distance to all individual harmonic waves $\{\boldsymbol{\Psi}_s\}$. Following our previous work (Chen et al., 2020a), we formulate the objective function as:

$$\begin{aligned} &\min_{\{\boldsymbol{\Psi}_s\},\bar{\boldsymbol{\Psi}}} F_{\{\boldsymbol{\Psi}_s\},\bar{\boldsymbol{\Psi}}} = \min_{\{\boldsymbol{\Psi}_s\},\bar{\boldsymbol{\Psi}}} \sum_{s=1}^{m} \left\{ tr\left(\boldsymbol{\Psi}_s^T \boldsymbol{L}_s \boldsymbol{\Psi}_s\right) + \lambda\left(P - tr\left(\boldsymbol{\Psi}_s^T \bar{\boldsymbol{\Psi}}\right)\right)\right\} \\ &s.t.\ \forall s : \boldsymbol{\Psi}_s^T \boldsymbol{\Psi}_s = \boldsymbol{I}_P \end{aligned} \tag{3}$$

where λ stands for the scalar balancing topological structure and centralization degree in Eq. (3).

Specifically, the first term requires each set of individual harmonic waves to retain the topological information derived from the Laplacian matrix $\boldsymbol{L}_s$. The second term is the geodesic distance constraint that ensures the global common harmonic waves $\bar{\boldsymbol{\Psi}}$ is close to all individual harmonic waves $\{\boldsymbol{\Psi}_s\}$ on the Stiefel manifold. The geodesic distance between $\boldsymbol{\Psi}_s$ and $\bar{\boldsymbol{\Psi}}$ is measured by a distance function (Chikuse, 2012) $d^2(\boldsymbol{\Psi}_s, \bar{\boldsymbol{\Psi}}) = 1/2 tr(\boldsymbol{\Psi}_s - \bar{\boldsymbol{\Psi}})^T(\boldsymbol{\Psi}_s - \bar{\boldsymbol{\Psi}}) = P - tr(\boldsymbol{\Psi}_s^T \bar{\boldsymbol{\Psi}})$. The orthogonal constraint term $\boldsymbol{\Psi}_s^T \boldsymbol{\Psi}_s = \boldsymbol{I}_P (\forall s)$ in Eq. (3) ensures that each individual harmonic waves $\boldsymbol{\Psi}_s$ is lying on the Stiefel manifold. We presented an alternative solution to optimize $\{\boldsymbol{\Psi}_s\}$ and the common global harmonic waves $\bar{\boldsymbol{\Psi}}$ using the manifold optimization technique (please see the optimization details in Section 2.5).

Similar to the Fourier bases in signal processing, harmonic waves have the limitation of global-ness. In many neuroimaging applications, biomarkers are expected to capture the local alterations that occur at particular brain regions. To overcome this limitation, we extend from the global harmonic wave to localized harmonic wavelets by adding the region-adaptive constraint to Eq. (2).

2.3. Construction of region-adaptive individual harmonic wavelets

To alleviate the limitation of global common harmonic waves $\bar{\boldsymbol{\Psi}}$, we propose the following three components to optimize the region-based individual harmonic wavelets $\boldsymbol{\Phi}_{s,i} \in \mathbb{R}^{N\times Q}$ ($Q < N$) for i^{th} node v_i of graph $\mathcal{G}_s$. As we will explain later, Q denotes the number of wavelet frequencies.

First, the region-based individual harmonic wavelets $\boldsymbol{\Phi}_{s,i}$ should preserve the locality of the topological structure, and this can be achieved by minimizing a harmonic energy $E_e(\boldsymbol{\Phi}_{s,i}) = tr(\boldsymbol{\Phi}_{s,i}^T \boldsymbol{L}_s \boldsymbol{\Phi}_{s,i})$, satisfying $\boldsymbol{\Phi}_{s,i}^T \boldsymbol{\Phi}_{s,i} = \boldsymbol{I}_Q$.

Second, the support of each individual harmonic wavelets $\boldsymbol{\Phi}_{s,i}$ does not expand more than a subnetwork centered at the underlying node v_i of graph $\mathcal{G}_s$. To relieve the task, we introduce a binary mask $u_{s,i} = [u_{s,i}(j)]_{j=1}^{N}$ as a slack vector, with $u_{s,i}(j) = 1$ representing the node v_j can be reached by the node v_i within k jumps and $u_{s,i}(j) = 0$ otherwise. It is worth noting that we use the shortest path to measure the distance between two nodes v_i and v_j, based on a binarized edge map via thresholding on adjacency matrix $\boldsymbol{W}_s$. A harmonic localization term is defined by $E_l(\boldsymbol{\Phi}_{s,i}) = tr(\boldsymbol{\Phi}_{s,i}^T diag(1 - u_{s,i}) \boldsymbol{\Phi}_{s,i})$. The minimizing $E_l(\boldsymbol{\Phi}_{s,i})$ is equivalent to encourage ${\boldsymbol{\Phi}_{s,i}}^2$ to be zero out of the subnetwork. The localization term E_l is used to suppress the waves (oscillation) far from v_i while preserve the waves nearby v_i, since $diag(1 - u_{s,i})$ is zero for the nodes closely connected to v_i within k jumps and has no effect in minimizing E_l.

Third, to achieve complementary characterizing the network by both the global common harmonic waves $\bar{\boldsymbol{\Psi}}$ and each region-adaptive individual harmonic wavelets $\boldsymbol{\Phi}_{s,i}$, they are penalized for being orthogonal via constraint $\boldsymbol{\Phi}_{s,i}^T \bar{\boldsymbol{\Psi}} = 0$. However, training of each individual harmonic wavelet to satisfy the orthogonality is computationally expensive. We relax it alternatively by promoting the orthogonality to the subspace spanned by $\bar{\boldsymbol{\Psi}}$, through minimizing $E_p = tr(\boldsymbol{\Phi}_{s,i}^T \bar{\boldsymbol{\Psi}} \bar{\boldsymbol{\Psi}}^T \boldsymbol{\Phi}_{s,i})$.

Finally, the whole energy function of identifying region-adaptive individual harmonic wavelets $\boldsymbol{\Phi}_{s,i}$ for node v_i of graph $\mathcal{G}_s$ is formulated as:

$$\begin{aligned} &\min_{\boldsymbol{\Phi}_{s,i}} F_{\boldsymbol{\Phi}_{s,i}} = \min_{\boldsymbol{\Phi}_{s,i}} E_e(\boldsymbol{\Phi}_{s,i}) + \mu_1 E_l(\boldsymbol{\Phi}_{s,i}) + \mu_2 E_p(\boldsymbol{\Phi}_{s,i}) \\ &s.t.\ \ \boldsymbol{\Phi}_{s,i}^T \boldsymbol{\Phi}_{s,i} = \boldsymbol{I}_Q \end{aligned} \tag{4}$$

where μ_1 and μ_2 are two scalars that balance the strength of subnetwork localization and redundancy with the global common harmonic waves $\bar{\boldsymbol{\Psi}}$. The detail of optimizing Eq. (4) is given in Section 2.5.

2.4. Identification of region-adaptive common harmonic wavelets

Similar to the motivation of constructing global common harmonic waves $\bar{\boldsymbol{\Psi}}$ for group comparison, we go one step further

Table 1
Algorithm for identifying region-adaptive common harmonic wavelets.

Parameters: λ; μ_1; μ_2;	
Input:	**Adjacency matrix** $\boldsymbol{W_s} \in \mathbb{R}^{N\times N}$, $s = 1, 2, \cdots, m$
Init.	Calculate Laplacian matrix $\boldsymbol{L_s} = \boldsymbol{D_s} - \boldsymbol{W_s}$, where $\boldsymbol{D} = \boldsymbol{D}(i,i) = \sum_{j=1}^{N} w_{ij}$; Initialize orthogonal matrix $\boldsymbol{\Psi}_s$ through the Eigen-decomposition of Laplacian matrix $\boldsymbol{L}_s$; Initialize parameter $\lambda = 0.005$, $\mu_1 = 10$ and $\mu_2 = 30$;
Step 1:	Optimize the global common harmonic waves $\bar{\boldsymbol{\Psi}}$ from a population of individual harmonic waves $\{\boldsymbol{\Psi}_s\}$ by solving the energy function Eq. (3) in two alternative steps.
Step 2:	Construct the region-adaptive individual harmonic wavelets $\boldsymbol{\Phi}_{s,i}$ for node $\boldsymbol{v}_i$ of graph $\mathcal{G}_s$ by solving the Eigen-decomposition of matrix $\boldsymbol{\Theta}_{s,i}$ in Eq. (6).
Step 3:	Identify the region-adaptive common harmonic wavelets $\bar{\boldsymbol{\Phi}}_i$ from the whole region-adaptive individual harmonic wavelets $\{\boldsymbol{\Phi}_{s,i} \vert s = 1, \cdots, m\}$ at node $\boldsymbol{v}_i$ by solving the Fréchet mean in Eq. (5) on the Stiefel manifold.
Output	**Region-adaptive common harmonic wavelets** $\{\bar{\boldsymbol{\Phi}}_i \vert i = 1, \cdots, N\}$

to infer the common harmonic wavelets $\bar{\boldsymbol{\Phi}}_i$ for node v_i , which describes the shared local network topology across individuals. Given a set of individual harmonic wavelets $\{\boldsymbol{\Phi}_{s,i} \vert s = 1, \cdots, m\}$ obtained by Eq. (4), discovering the region-adaptive common harmonic wavelets $\bar{\boldsymbol{\Phi}}_i$ implies for estimating the manifold mean, which has the shortest geodesic distances to all the observed instances $\{\boldsymbol{\Phi}_{s,i}\}$ residing on the Stiefel manifold. Here, we reuse the Stiefel manifold distance from Section 2.2 and formulate the objective function of finding common harmonic wavelets associated with the node v_i as:

$$\min_{\bar{\boldsymbol{\Phi}}_i} F_{\bar{\boldsymbol{\Phi}}_i} = \min_{\bar{\boldsymbol{\Phi}}_i} \sum_{s=1}^{m} d^2\left(\boldsymbol{\Phi}_{s,i}, \bar{\boldsymbol{\Phi}}_i\right) = \min_{\bar{\boldsymbol{\Phi}}_i} \sum_{s=1}^{m} \left(Q - tr\left(\boldsymbol{\Phi}_{s,i}^T \bar{\boldsymbol{\Phi}}_i\right)\right) \tag{5}$$

One possible solution to Eq. (5) is the classic Fréchet mean. We present the optimization of Eq. (5) in Section 2.5. Compared with the global common harmonic waves $\bar{\boldsymbol{\Psi}}$, the harmonic wavelets $\{\bar{\boldsymbol{\Phi}}_i \vert i = 1, \ldots, N\}$ are specific to each brain region v_i. Thus, such region-adaptive harmonic wavelets act like "swiss army knife" of the network topology, allowing us to precisely characterize the complex neurodegeneration process that differentially affects brain regions.

2.5. Optimization

Our framework mainly consists of three energy functions, including estimation of global common harmonic waves, construction of region-adaptive individual harmonic wavelets, and optimization of region-adaptive common harmonic wavelets. Since the involved variables are the instance of the Stiefel manifold, we propose the following manifold-based optimization methods. The whole optimization framework is briefly summarized in Table 1 with the computational and space complexity analyses introduced in **Suppl. S1**.

2.5.1. Optimizing the global common harmonic waves in two alternative steps

Given that it is computationally expensive to estimate individual and common harmonic waves jointly in Eq. (3), we propose the gradient descent manifold optimization under the framework of ADMM (Alternating Direction Method of Multipliers) (Boyd et al., 2011). Specifically, our numerical solution iteratively alternates two steps until convergence. (1) *Adjust each individual-based harmonic wave toward the latent manifold center.* Each individual harmonic waves $\boldsymbol{\Psi}_s$ is not only influenced by the topological structure of its own Laplacian matrix $\boldsymbol{L}_s$ but also attracted by the latent common harmonic waves. (2) *Estimate the global common harmonic waves.* Fixing the individual harmonic waves $\{\boldsymbol{\Psi}_s\}$ obtained from step 1, we first project each $\boldsymbol{\Psi}_s$ to the tangent space at the current common harmonic waves. Then, we calculate the mean tangent which points to the new location of manifold center on the tangent plane. Next, we map the mean tangent back to the Stiefel manifold to obtain the new manifold center estimation (latent common harmonic waves), which is used for guiding the refinement of individual harmonic waves in step 1. Please refer to our recent work (Chen et al., 2020a) for detail.

2.5.2. Constructing the region-adaptive individual harmonic wavelets by Eigen-decomposition

Due to the linearity of the trace, it is clear that three trace terms in Eq. (4) can be unified into one trace term with a matrix $\boldsymbol{\Theta}_{s,i} = \boldsymbol{L}_s + \mu_1 diag(1 - \boldsymbol{u}_{s,i}) + \mu_2 \bar{\boldsymbol{\Psi}} \bar{\boldsymbol{\Psi}}^T$. Thus, the optimization of Eq. (4) is boiled down to the eigen-decomposition of the matrix $\boldsymbol{\Theta}_{s,i}$:

$$\underset{\boldsymbol{\Phi}_{s,i}}{\operatorname{argmin}}\, tr\left(\boldsymbol{\Phi}_{s,i}^T \boldsymbol{\Theta}_{s,i} \boldsymbol{\Phi}_{s,i}\right) \quad s.t.\ \boldsymbol{\Phi}_{s,i}^T \boldsymbol{\Phi}_{s,i} = \boldsymbol{I}_Q \tag{6}$$

Since $\boldsymbol{\Theta}_{s,i}$ is symmetric and positive semi-definite, it is computationally efficient to obtain $\boldsymbol{\Phi}_{s,i}$ for each node $\boldsymbol{v}_i$ of graph $\mathcal{G}_s$.

2.5.3. Learning the region-adaptive common harmonic wavelets on the Stiefel manifold

As with the second step of optimizing the global common harmonic waves, given the region-adaptive individual harmonic wavelets $\{\boldsymbol{\Phi}_{s,i} \vert s = 1, \cdots, m\}$ for all graph $\{\mathcal{G}_s\}$ at node $\boldsymbol{v}_i$, the optimization $\{\bar{\boldsymbol{\Phi}}_i\}$ of Eq. (5) falls into the classic problem of solving the Fréchet mean on the Stiefel manifold, which can be effectively solved by adopting the Weiszfeld algorithm (Aftab et al., 2014).

2.5.4. Hyper-parameter pruning

Our proposed framework for identifying the region-adaptive common harmonic wavelets contains two types of parameters: harmonic dimension (P and Q) and hyperparameters (λ, μ_1, and μ_2). Regarding the dimension reduction, we determine the dimension P for each individual-based harmonic waves $\boldsymbol{\Psi}_s$ based on the reconstruction error between the observed Laplacian matrix $\boldsymbol{L}_s$ and the reconstructed Laplacian matrix using only the top P smallest eigenvalues and eigenvectors. Generally, we select the P as the stable point such that the decrease of reconstruction error is marginal as P increases. In addition, the dimension Q of region-adaptive individual harmonic wavelets $\boldsymbol{\Phi}_{s,i}$ is empirically set based on the average node degree of all adjacency matrices. Regarding the hyperparameter selection, we adopt a grid search strategy to determine the optimal value of parameter λ, μ_1 and μ_2 based on the signal reconstruction loss on real data, which is presented in Section 3.1. In the following experiments, we set the dimensions P and Q to 55 and 10, respectively. In terms of hyperparameters, we select $\lambda = 0.005$, $\mu_1 = 10$ and $\mu_2 = 30$ as the optimal parameters, which achieve the lowest signal reconstruction loss. We give the details of evaluating the impact of hyper-parameters in **Suppl. S2**.

2.6. Application of harmonic wavelets analysis

Traditional neuroimaging studies usually adopt empirical biomarkers such as amyloid deposition and tau tangle aggregation to investigate the neuropathological mechanism of Alzheimer's disease. In this work, we propose a novel harmonic wavelet analysis to discover the spatial-spectrum alterations that are associated with the local propagation patterns of neuropathological burdens across brain networks. We use the learned common harmonic

wavelets $\{\bar{\mathbf{\Phi}}_i\}$ to characterize the graph-eigen-adaptive representations (GEAR in short) for each instance of empirical biomarkers (such as amyloid) $f \in \mathbb{R}^N$ by:

$$\hat{h}_{i,q} = \left|\hat{\alpha}_{i,q}\right|^2 = \left|f, \bar{\varphi}_{i,q}\right|^2 \tag{7}$$

where each element in vector f represents the regional biomarker level. The intuition behind GEAR $\hat{h}_{i,q}$ is essentially the harmonic energy of spreading the neuropathology burden f through the underlying wavelet $\bar{\varphi}_{i,q}$ at the region v_i. The harmonic power $\hat{\alpha}_{i,q}$ characterizes the momentum (speed) of propagation for each self-organized oscillation pattern across localized subnetwork centered on the region v_i. In Section 3, we will demonstrate that our spatial-spectrum representations achieve enhanced performance in stratifying CN, EMCI, and LMCI, compared with current empirical biomarkers.

3. Experiments

After describing the neuroimaging data in Section 3.1, we first test the representation power of harmonic wavelets by decomposing the graph signal and reconstructing it back to the signal domain in Section 3.2. Then, we evaluate the replicability of region-adaptive common harmonic wavelets using our proposed algorithm via the resampling test in Section 3.3. Next, we investigate the diagnostic ability of our spatial-spectrum representations in stratifying aging subjects into the pre-clinical stage of AD in Section 3.4. Finally, we evaluate our proof-of-concept application in AD study that the pathological events spreading in the context of white matter wiring exhibit ubiquitous oscillation patterns which can be captured by the optimized harmonic wavelets.

3.1. Data description

3.1.1. Training data for identifying the region-adaptive common harmonic wavelets

Here, we collect neuroimaging data of 138 subjects with T1-weighted MR and DWI images from the ADNI database (http://adni.loni.usc.edu/). We apply the following major image processing steps to construct the structural brain network. First, we reconstruct and parcellate the cortical white matter surface into 148 regions using Destrieux atlas (Destrieux et al., 2010) based on the T1-weighted MR images via FreeSurfer. Then, we apply surface seed-based probabilistic fiber tractography (Destrieux et al., 2010) to the DWI images via FSL, thus producing a 148×148 anatomical connectivity matrix $\boldsymbol{W}_s$, where the weight of the anatomical connectivity of pair-wise regions is the whole brain ratio of the number of fibers between the regions. Finally, we apply our proposed harmonic wavelet learning method on these 138 adjacency matrices $\{\boldsymbol{W}_s | s = 1, \cdots, 138\}$ to identify the region-adaptive common harmonic wavelets $\{\bar{\mathbf{\Phi}}_i | i = 1, \cdots, 148\}$.

3.1.2. Testing data for discovering the spatial-spectrum alterations in AD

After obtaining the harmonic wavelets $\{\bar{\mathbf{\Phi}}_i\}$, we select another dataset from ADNI for the group comparison analysis, where the imaging modalities include amyloid-PET and tau-PET. The statistical information of the testing data is shown in Table 2. We apply the same data processing pipeline to parcellate the cortical surface into the 148 structural brain regions and then calculate the standard update value ratio (SUVR) of PET imaging for each region, where the cerebellum is used as the reference in calculating the SUVR.

3.2. Evaluating the representation power of harmonic wavelets

In this section, we examine the representation power of the learned harmonic wavelets by evaluating the reconstruction effort of a graph signal running on the simulated brain network. Specifically, we first synthesize a brain network with 30 nodes and then randomly generate a graph signal f with each element representing the signal strength of node, ranging from -1 to $+1$, as shown in Fig. 3(a). Then, the reconstruction loss of f can be calculated by $(f - \bar{\mathbf{\Psi}}\bar{\mathbf{\Psi}}^T f)$ with the global harmonic waves $\bar{\mathbf{\Psi}}$. Since we select the first P eigenvectors, i.e., $\bar{\mathbf{\Psi}} \in \mathbb{R}^{N \times P} (P < N)$, the residual signal after reconstruction using the first 20 $(P = 20)$ harmonic waves is displayed in Fig. 3(b), where red and blue arrows stand for positive and negative residuals, respectively. Furthermore, we show the histogram of residuals in the top right corner.

As mentioned in Section 2.3, the harmonic wavelets $\bar{\mathbf{\Phi}}_i$ at each node v_i are the complementary bases to the global harmonic waves $\bar{\mathbf{\Psi}}$. In this context, we can reconstruct the signal value at each node v_i by $\tilde{f}_i = \bar{\mathbf{\Psi}}\bar{\mathbf{\Psi}}^T (f \odot u_i) + \bar{\mathbf{\Phi}}_i \bar{\mathbf{\Phi}}_i^T f$, where $\odot$ is the Hadamard product and u_i is the subnetwork mask vector centered at the node v_i. The first term quantifies the global reconstruction of truncated signal $f \odot u_i$ at node v_i, where we set $P = 20$. In addition, the second term is the localized reconstruction component, where we set $Q = 5$. Therefore, the reconstruction loss can be estimated by $(f - \tilde{f})$, where the residual signal and the corresponding histogram of reconstruction loss are shown in Fig. 3(d). It is clear that our harmonic wavelets have significantly smaller reconstruction loss compared with using global harmonic waves only. For the sake of fairness, we re-estimate the reconstruction loss by expanding the number of harmonic waves, i.e., increasing P from 20 to 25, which has the equal total number of bases as our harmonic wavelets ($P = 20$, $Q = 5$). As shown in Fig. 3(c), however, the reconstruction loss is still worse than our harmonic wavelets, indicating our harmonic wavelets can more effectively characterize the local network topology than the counterpart of global harmonic waves. Moreover, we compare the reconstruction performance of the learned harmonic wavelets with global harmonic waves under various noise contaminations on simulated data (as shown in **Suppl. S3**). The experimental results demonstrate that the harmonic wavelets achieve the best reconstruction performance when the noise contamination is low. However, the harmonic wavelets are susceptible to noise contamination, since they can characterize the local network topology and capture the details of the graph signal.

Using the similar reconstruction procedure, we evaluate the reconstruction loss of regional amyloid and tau levels, where the average reconstruction loss by using 55 global harmonic waves, 60 global harmonic waves, and our region-adaptive harmonic wavelets ($P = 55$, $Q = 10$) are displayed in blue, red, and green, respectively, in Fig. 3(e-f). All reconstruction loss on two AD biomarkers demonstrates that our harmonic wavelets achieve better representation power than global harmonic waves, where the improvements are statistically significant under t-test ($p < 0.01$).

3.3. Evaluating the replicability of common harmonic wavelets

Here, we estimate the robustness of the learned common harmonic wavelets through a replicability test. Specifically, we apply the following resample procedure to generate 50 test/retest datasets from the training data: (1) randomly sample 95 brain networks from the 138 training brain networks; (2) continue to sample another two sets of networks from the remaining 43 subjects separately, each with 5 networks; (3) form two paired cohorts by combining the networks sampled in step 1 and 2. Then, we apply our proposed method to two datasets independently. Thus, we have 50 samples of harmonic wavelets for the test dataset and another 50 samples for the retest dataset. Since two paired cohorts only have 5% (5/100) differences in terms of network data, we can evaluate the replicability of our method by testing whether there exists a significant difference ($p < 0.01$) at each coefficient

Table 2
Statistics of testing data in our experiments.

Data	Gender	Number	Range of Age	Average Age	CN	EMCI	LMCI
Amyloid	Male	450	55.0∼91.4	73.4	136	184	130
	Female	389	55.0∼89.6	71.7	148	145	96
	Total	**839**	**55.0∼91.4**	**72.6**	**284**	**329**	**226**
Tau	Male	207	55.0∼90.1	72.4	76	69	62
	Female	173	55.0∼89.9	70.3	81	44	48
	Total	**380**	**55.0∼90.1**	**71.3**	**157**	**113**	**110**

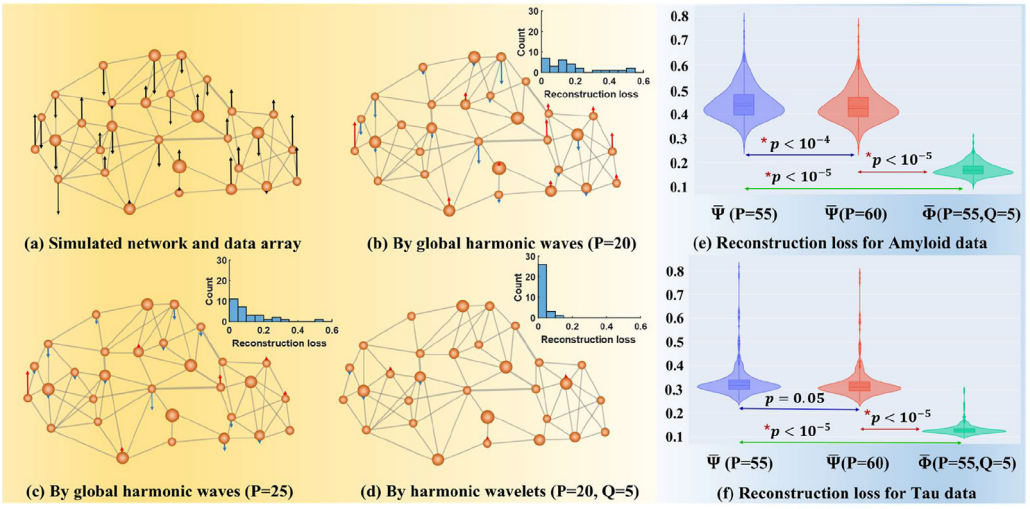

Fig. 3. Representation power comparison between global harmonic wave and our region-adaptive harmonic wavelets in simulated data (left) and A-T biomarker data (right). (a) The simulated network and one graph signal (displayed in arrows). (b-d) The reconstruction loss on simulated data using global harmonic waves $\bar{\Psi}(P = 20)$, global harmonic waves $\bar{\Psi}(P = 25)$, and our harmonic wavelets $\bar{\Phi}(P = 20$ and $Q = 5)$. (e) The reconstruction loss on amyloid-PET and tau-PET data on the brain network with 148 nodes by global harmonic waves $\bar{\Psi}(P = 55)$ in blue, global harmonic waves $\bar{\Psi}(P = 60)$ in red, and our harmonic wavelets $\bar{\Phi}(P = 55, Q = 5)$ in green, where '*' denotes statistical significance ($p < 0.01$).

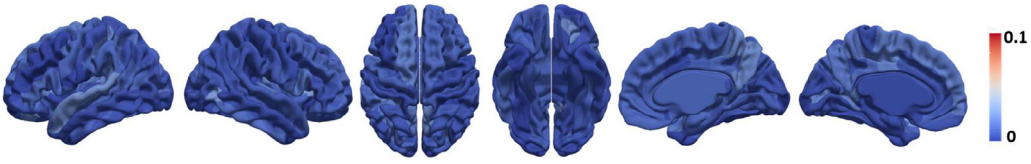

Fig. 4. Replicability test of our common harmonic wavelets, where the chance of failing replicability test at each brain cortical region is color-coded using the colormap in the right.

in harmonic wavelet matrix for each node via the paired t-test. Fewer elements showing significance indicate better replicability at each node. Since the harmonic wavelets are associated with brain regions, we count the number of wavelet coefficients that fail the replicability testing and normalize it by the total amount of wavelet coefficients at each region. Then, we display such a ratio at each brain cortical region in Fig. 4. It is apparent that the wavelet coefficients pass the replicability test in most brain regions, indicating the estimated common harmonic wavelets are consistent across individuals.

3.4. Evaluating the statistical power of GEAR biomarker based on common harmonic wavelets

In this experiment, we estimate the statistical power of our GEAR (Eq. (7)) in stratifying the CN, EMCI, and LMCI. Since the region-wise SUVR extracted from amyloid-PET and tau-PET have been widely used in neuroimaging studies, we compare our GEAR biomarkers with these empirical biomarkers through the following two tests.

In the first experiment, we build on three group comparisons (CN/EMCI, CN/LMCI, and EMCI/LMCI) of A and T biomarkers to identify the node alterations using empirical SUVR and GEAR. Regarding the empirical biomarkers, we apply the general linear model (GLM) to predict diagnostic labels using SUVR at each node, where age and gender are confounders. Regarding the new GEAR biomarker, since there are ten harmonic wavelets at each node, we apply the GLM to these ten harmonic wavelets, where the group difference at each brain region depends on the smallest p value across the spectrum of the GEAR biomarkers at the underlying node. In both statistical tests, all the p values are corrected using False Discovery Rate by Benjamini-Hochberg (BH) (Benjamini and Hochberg, 1995) since we assume each node is not completely independent of other nodes in the brain network.

In the second experiment, we test the diagnostic potential of our GEAR and empirical SUVR by estimating the accuracy of the early diagnosis of AD in the pre-clinical stage. Specifically, we use the SUVR data and GEAR biomarkers as input to train the linear support vector machine (SVM) classifier separately. Then we evaluate the Area Under the Receiver Operating Characteristic (AUROC)

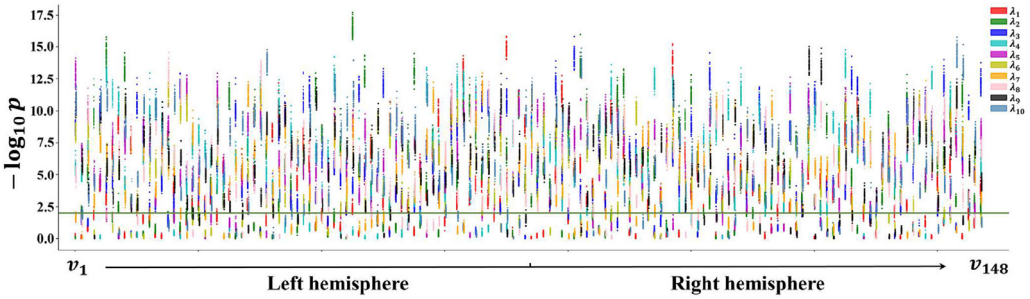

Fig. 5. The Manhattan plot of significant values of harmonic wavelets in CN/LMCI comparison on Amyloid data.

and Area Under the Precision-Recall curve (AUPR) score using 10-fold cross-validation.

3.4.1. A-biomarker: amyloid SUVR vs. amyloid GEAR

In the group comparison experiment, we find that amyloid SUVR has identified one brain region (*inferior frontal gyrus*) exhibiting a significant difference in CN/EMCI and no significant regions in EMCI/LMCI comparison. In contrast, our amyloid GEAR biomarker finds in total 43 and 9 nodes showing significant difference between CN/EMCI and EMCI/LMCI cohorts with FDR-adjusted $p < 10^{-5}$. Besides, only one region (*rectus gyrus*) manifests CN/LMCI difference using amyloid SUVR, while 29 brain regions show CN/LMCI difference using amyloid GEAR (FDR-adjusted $p < 10^{-14}$). These results imply our amyloid GEAR biomarker achieves higher statistical power in identifying disrupted regions than the empirical neuroimaging biomarkers.

Since there are multiple harmonic wavelets associated with each brain region, we go one step further to evaluate the statistical power of all harmonic wavelets (at different brain regions and across graph spectrum) by taking CN/LMCI comparison as an example. First, we randomly select 90% of samples in CN and LMCI groups to calculate the FDR-adjusted p value for each harmonic wavelet at each region. We repeat this process 50 times. Fig. 5 shows the Manhattan plot of significant value (negative log-transformation of FDR-adjusted p value) for each harmonic wavelet, where we use different colors to indicate the frequency of harmonic wavelet. It is clear that the majority body of the harmonic wavelets show competitive power in separating CN and LMCI groups (FDR-adjusted $p < 0.01$), as most of the p-values are above the green reference line ($-\log_{10}0.01$).

Recall we have identified 29 brain regions showing significant CN/LMCI difference using GEAR biomarker. Here, we focus on the harmonic wavelets associated with these 29 brain regions (displayed in Fig. 6(a)). First, we plot the p-values of each harmonic wavelet at each region (horizontal axis) and across harmonic frequencies (vertical axis) in Fig. 6(d), where the color and size of each circle reflect the significance level (in $-\log_{10}p$). Furthermore, we show the average of GEAR biomarker from lowest (λ_1) to the highest (λ_{10}) frequency for CN and LMCI groups in Fig. 6(b), respectively. To measure the separation between CN and LMCI groups, the Fisher score J_F (ratio between inter-class mean and intra-class variance) of the GEAR biomarker between CN and LMCI subjects is also shown in the outermost ring in Fig. 6(b). In addition, we measure the whole-brain GEAR biomarker level of amyloid for each subject and plot its distribution for CN (in red) and LMCI (in blue) subjects in Fig. 6(c). These results suggest that the increment of amyloid deposition raises the harmonic energy of the brain network, which eventually leads to less stable system status.

In Fig. 6(b), it is apparent that the harmonic-based alterations have the preference to affect the medium frequency spectrum. It is also evidenced by the fact that the harmonic wavelets with the smallest p-values are all associated with medium frequencies. Since each harmonic wavelet exhibits ubiquitous oscillation patterns on the brain network, we conceptualize that such oscillation patterns of each identified significant harmonic wavelet might be overlapped with the spreading pathway of amyloid plaque throughout the brain network. The in-depth discussion on the neuroscience insight of this hypothesis can be found in Section 3.5. Here, we set the stage to visualize the harmonic wavelets with the top three strongest statistical differences (smallest p-values) in Fig. 7, where the red dot denotes the underlying node, and the red/blue arrows indicate the positive/negative oscillations in each harmonic wavelet.

Furthermore, we evaluate the diagnostic potential of identified significant amyloid SUVR and amyloid GEAR biomarkers by training a linear SVM classifier for CN/EMCI/LMCI classification separately. We use 10-fold cross-validation to evaluate the classification results (AUROC and AUPR), as shown in Fig. 8, where the '*' indicates that the classification performance of our GEAR is significantly better than that of the empirical SUVR. It is apparent that our amyloid GEAR consistently achieves significantly higher classification performance compared with empirical amyloid SUVR in three classification tasks. These results demonstrate our proposed region-adaptive common harmonic wavelet technique has great potential in the early diagnosis of AD.

3.4.2. T-biomarker: tau SUVR vs. tau GEAR

Similar to the experiments in Section 3.4.1, we first apply node-wise group comparison using tau SUVR and tau GEAR biomarker. Five brain regions exhibit EMCI vs. LMCI difference using tau SUVR, compared to 20 regions showing significant group difference using tau GEAR biomarker, both after FDR-correction ($p < 10^{-5}$). In addition, both tau SUVR and GEAR biomarkers have 24 regions showing significant CN/LMCI difference (FDR-adjusted $p < 10^{-9}$), although the spatial locations of the identified brain regions are slightly different. Note, we find five brain regions survive from the significant testing between CN and EMCI cohorts using tau GEAR biomarker, while none of the brain regions shows significant difference using tau SUVR (FDR-adjusted $p < 0.01$).

Fig. 9 shows the Manhattan plot of p-value (negative log-transformation of FDR-adjusted p value) for all harmonic wavelets (148 regions $\times$ 10 harmonic frequencies) in CN/LMCI group comparison, where most of the harmonic wavelets outperform the reference line (i.e., $p < 0.01$) in terms of statistical power. Since 24 brain regions (shown in Fig. 10(a)) have been identified manifesting significant group differences between CN and LMCI cohorts, we display the p-values of all the harmonic wavelets in these 24 regions (horizontal axis) across frequency (vertical axis) in Fig. 10(d), where larger and darker circle indicate smaller p-value. We also show the average tau GEAR for CN and LMCI cohorts in each harmonic frequency band in Fig. 10(b). The Fisher distance of mean harmonic energy in each frequency is displayed in the outermost

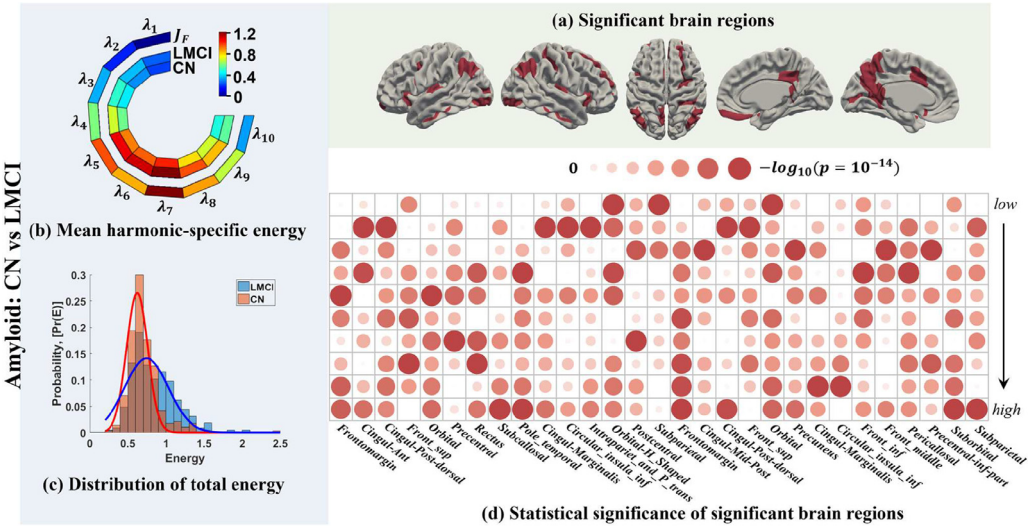

Fig. 6. The CN vs. LMCI group comparison using amyloid GEAR biomarkers for the 29 brain regions (a) showing significant differences, where we plot the negative log p-value for each harmonic wavelet at different regions (horizontal axis) and across frequency (vertical axis) in (d). In (b), we not only display the average harmonic energy in each harmonic frequency for CN and LMCI groups but also show the separation (measured by Fisher score) between CN and LMCI groups. In (c), we show the histogram of whole-brain harmonic energy for CN and LMCI groups in red and blue, respectively.

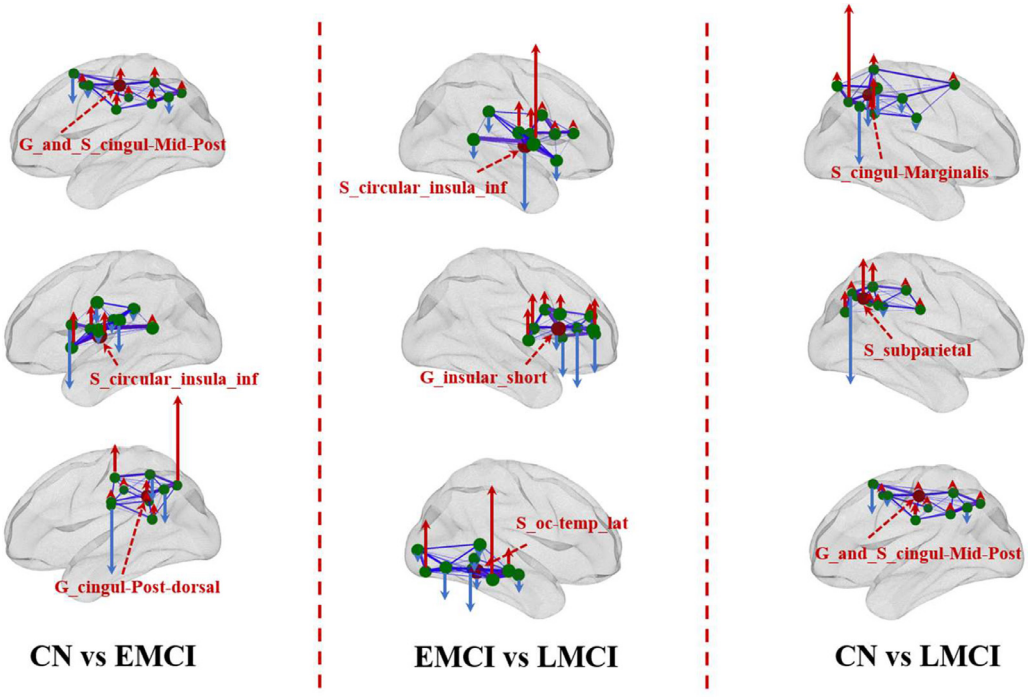

Fig. 7. The visualization of the top three significant harmonic wavelets associated with amyloid-PET in CN/EMCI (left), EMCI/LMCI (middle), and CN/LMCI (right) comparison. The underlying center node of the harmonic wavelet is denoted with a red dot. The up/down oscillation pattern in each wavelet is displayed by red/blue arrows.

ring plot in Fig. 10(b). Similar to the preference pattern of amyloid GEAR (Fig. 6), harmonic-based alterations by tau GEAR biomarker have the preference to affect the medium frequency spectrum. In Fig. 10(c), the histogram of whole-brain harmonic energy shows a similar trend as the amyloid GEAR that the higher level of tau pathology in the late-stage cohort yields a higher load of harmonic energy in the brain network system. The top three significant harmonic wavelets mapped on the cortical surface are also shown in Fig. 11. Moreover, the classification results of CN/EMCI, EMCI/LMCI, and CN/LMCI, using tau SUVR and GEAR are shown in Fig. 12, where our GEAR biomarker significantly outperforms tau SUVR on AUROC and AUPR scores ($p < 0.01$).

3.5. Discussion on the neuroscience insight of harmonic wavelets

Human brain is a complex system where each part of the brain is hierarchically interconnected. Although the pathophysiological mechanism of Alzheimer's disease is largely unknown, it is highly possible that the observed pathological burden does not appear randomly in the brain. Instead, we conceptualize that the spreading of pathological burden is governed by the wiring topology of the underlying brain network. In this context, the role of harmonic wavelets is acting as the predefined interference waves that can be used to computationally excite the brain network undergoing neuropathological events. Unique geometrical patterns are supposed to

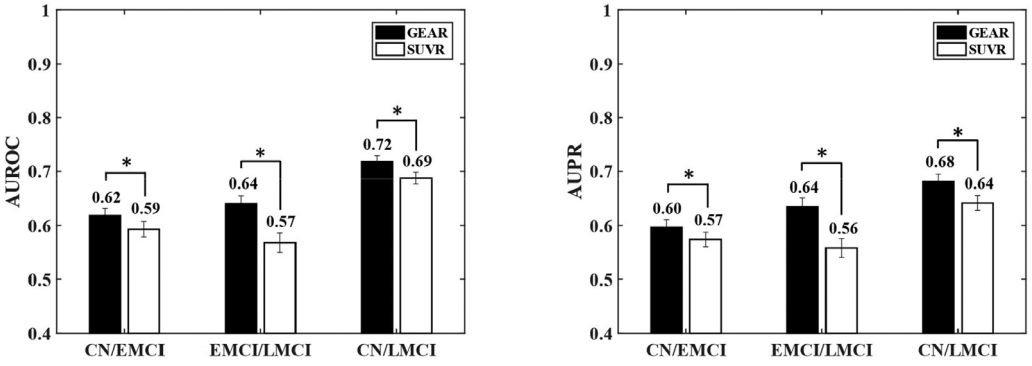

Fig. 8. The classification results of using amyloid SUVR and amyloid GEAR in CN/EMCI, EMCI/LMCI, and CN/LMCI comparison.

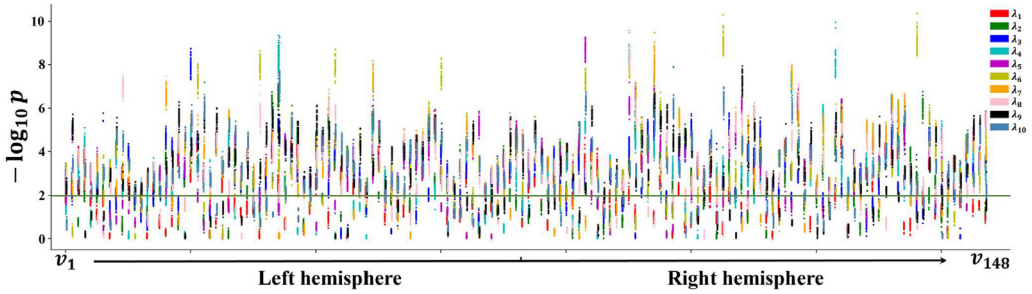

Fig. 9. The Manhattan plot of significant values of harmonic wavelets in CN/LMCI comparison using Tau GEAR biomarker.

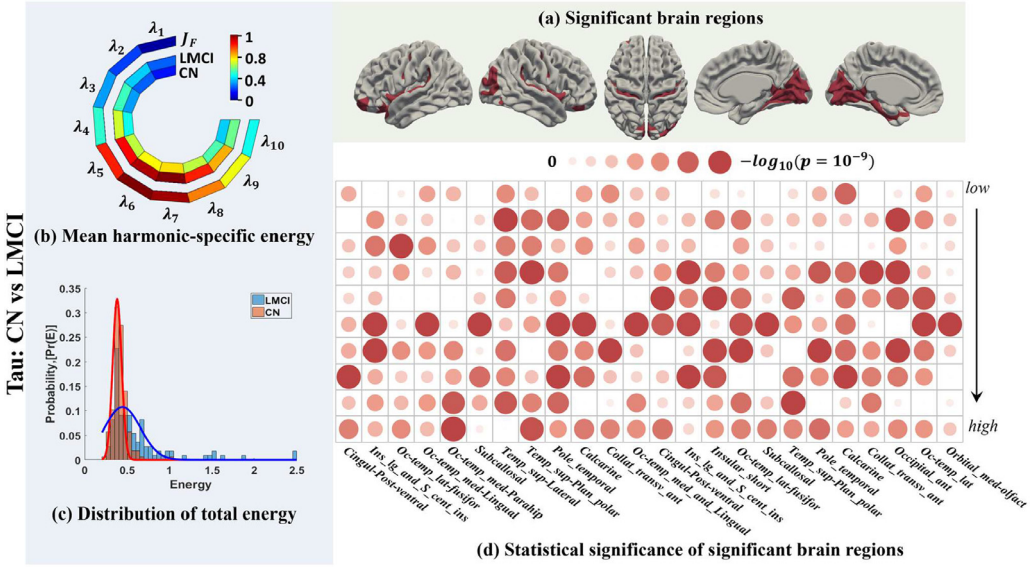

Fig. 10. The CN vs. LMCI group comparison using tau GEAR biomarkers for the 24 brain regions (a) showing significant differences, where we plot the negative log *p*-value for each harmonic wavelet at different regions (horizontal axis) and across frequency (vertical axis) in (d). In (b), we not only display the average harmonic energy in each harmonic frequency for CN and LMCI groups but also show the separation (measured by Fisher score) between CN and LMCI groups. In (c), we show the histogram of whole-brain harmonic energy for CN and LMCI groups in red and blue, respectively.

emerge in the excitatory waves, depending on the resonance between the spatial distribution of pathology in the brain and the frequency of harmonic wavelets.

Since each brain has a unique harmonic system, it is of high necessity to characterize and compare the individual's propagation patterns of AD-related neuropathology using the common harmonic wavelets. In Section 3.4, we have shown the brain regions that manifest harmonic alterations between different stages of AD progression. Fig. 13 further display the aggregated harmonic wavelets that pass the significance testing in each group comparison, where we show the oscillation patterns as well as its surface rendering for the left and right hemispheres, respectively. Here, we conceptualize each aggregated harmonic wavelet as the population-wise *resonance wave* that is supposed to synchronize with the spreading pathway of neuropathologies from the baseline to the more advanced stage. For instance, the resonance wave derived from the CN/EMCI comparison (Fig. 13 left) implies the spreading pathway of amyloid or tau in the CN cohort after the disease progresses to EMCI stage. It is apparent amyloid and tau have quite different resonance waves in the early stage of AD. However, the oscillation patterns become similar in the late MCI stage, as the similarity map shown in Fig. 14. Note, it makes more

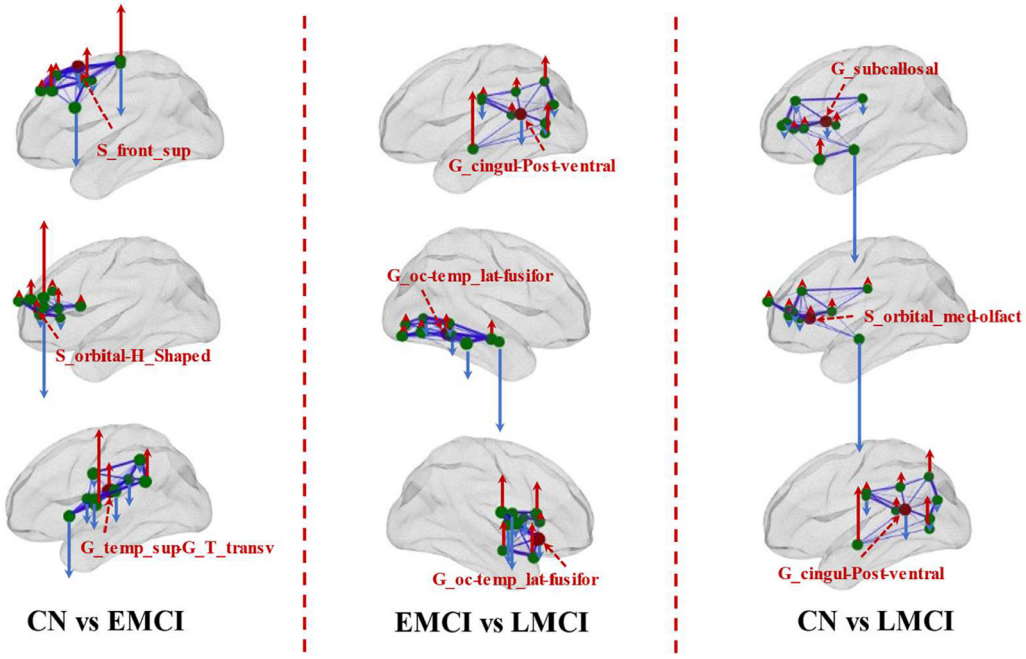

Fig. 11. The visualization of the top three significant harmonic wavelets in Tau-PET. We use the same symbols as Fig. 7 for the illustration of harmonic wavelets.

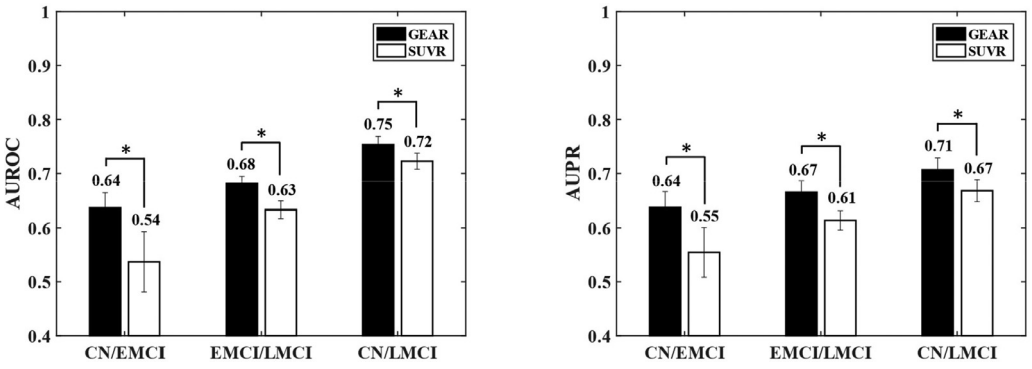

Fig. 12. The classification results of using tau SUVR and tau GEAR in CN/EMCI, EMCI/LMCI, and CN/LMCI comparison.

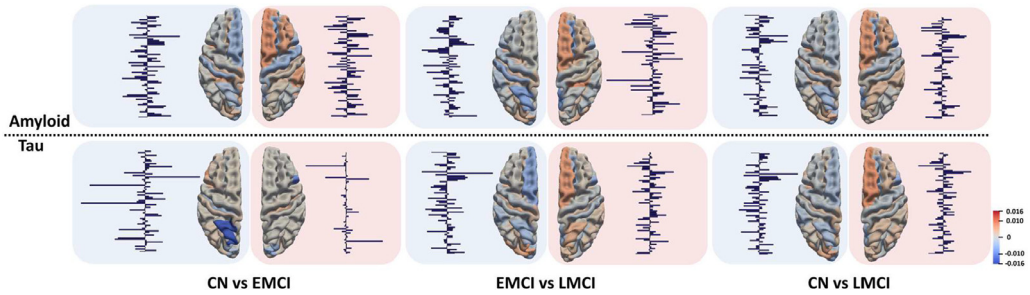

Fig. 13. The visualization of oscillation patterns of resonance waves of amyloid (top) and tau (bottom) in CN/EMCI, EMCI/LMCI, and CN/LMCI comparison.

sense to test this proof-of-concept approach on an individual basis using the longitudinal neuroimaging data. We leave this for our future work.

Since amyloid and tau are the hallmarks of AD, most current studies focus on the brain regions that exhibit high concentration levels. There is a converging consensus that an excessively large amount of pathology burden is a clear indicator of vulnerability in the brain that needs immediate attention in AD diagnosis or treatment (Mattson and Magnus, 2006; Saxena and Caroni, 2011; Wang et al., 2016). Inspired by the oscillation patterns in the harmonic waves, we would like to argue that brain regions actively involved in the spreading of neuropathologies are also critical to the cognitive decline in the neurodegeneration process. To support this argument, we provide the evidence in Fig. 15. Recall harmonic power (in Eq. (6)) can be used to quantify the spreading speed of the underlying harmonic wavelet. In general, fast oscillations yield a quick exchange of pathologies from one region to the other connected brain regions. The positive degree of harmonic power indicates the acceleration of the spreading process. On the contrary, the negative degree indicates the slow-

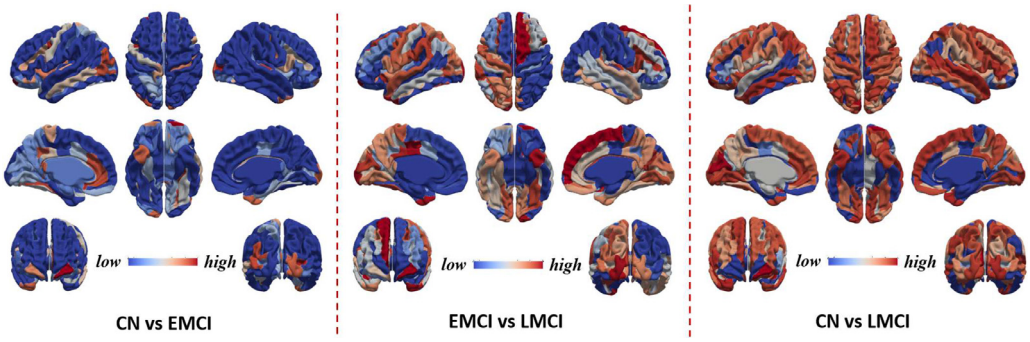

Fig. 14. The similarity map between amyloid and tau resonance waves as the disease progresses from the baseline to the more advanced stage.

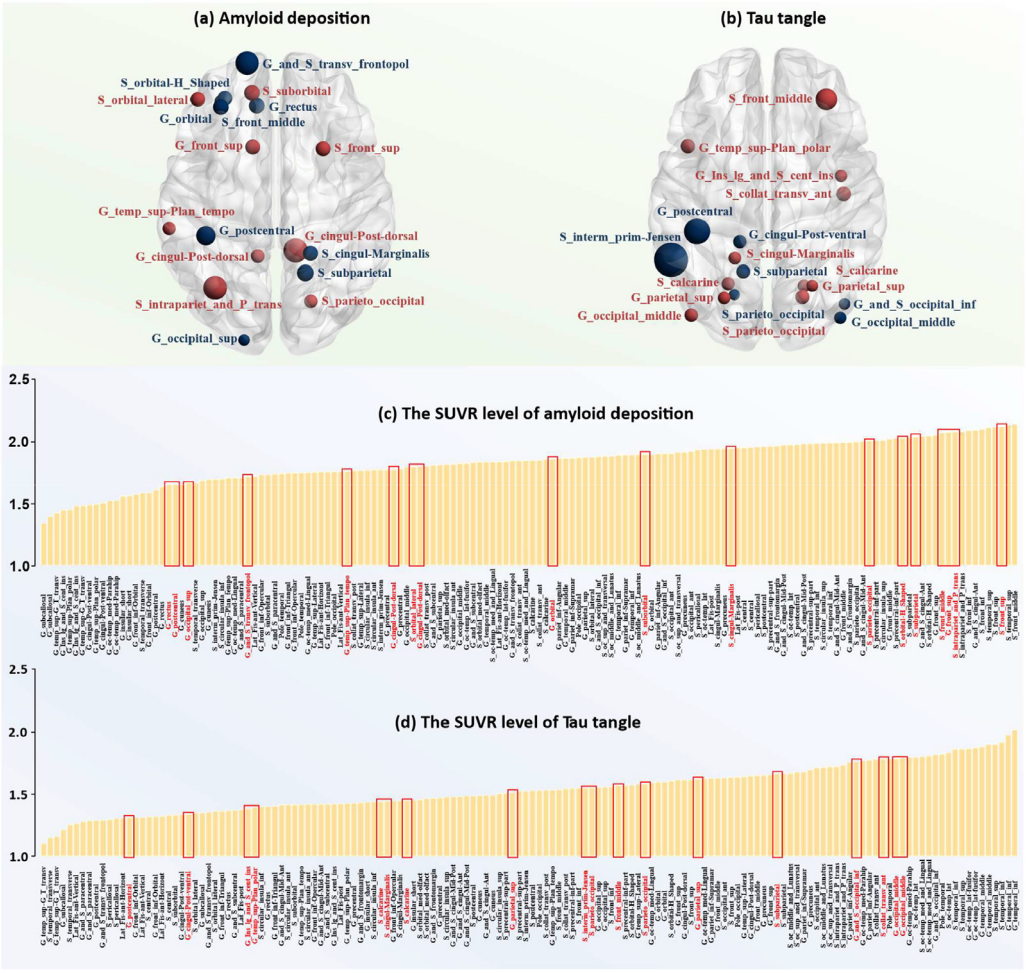

Fig. 15. Top: The illustration of critical brain regions for amyloid and tau biomarkers that show the strongest association between cognitive decline and harmonic power in GLM. The size and color of each node stand for the magnitude and sign of the slope in GLM. Bottom: The ranking of the SUVR degree of the identified brain regions in the brain.

down of speed in accumulating neuropathology. However, the total amount of pathological burden at the underlying brain region might keep increasing. Following this clue, we apply a GLM to each harmonic wavelet where the outcome is the change of MMSE score (Tombaugh and McIntyre, 1992) (difference between MMSE score taken at the last visit and baseline), and the predictor is the harmonic power measured at the baseline. Age, gender, and diagnostic label are confounders. After FDR correction ($p < 10^{-8}$), we visualize the power of harmonic wavelets at the 18 brain regions that manifest the strongest significance between cognitive decline (measured by MMSE change) and harmonic power in our GLMs for amyloid and tau in the top of Fig. 15, where the size of the node reflects the magnitude of slope (the effect size of harmonic power in GLM) and color indicates the sign of slope (red for positive and blue for negative). Furthermore, we examine the SUVR level of these identified brain regions (red boxes) at the bottom of Fig. 15, where we sort the SUVR degree in increasing order. It is interesting that a significant number of regions play a critical role in spreading the pathology in the brain, however, the concentration levels of pathology burden at these regions are not ranked at

the top in the brain. One possible explanation is that those brain regions shown in Fig. 15 are more inclined to transmit the pathology from one region to other regions in a prion-like manner rather than accumulating and retaining the pathology in a local region of the brain. Considering AD is a progressive neurodegenerative disease, our result shows the importance of studying critical regions in the brain which are responsible for cognitive decline due to the criticality in spreading the neuropathological burdens throughout the brain.

4. Conclusion

In this paper, we propose a proof-of-concept computational approach to capture the propagation patterns of AD-related neuropathological burdens using neuroimaging and network science technology. The backbone of our method is to find the region-adaptive common harmonic wavelets that allow us to adaptively characterize the spreading of pathological events localized at each brain region. To achieve it, we present a manifold-based optimization method to generate harmonic wavelets for each subject and then unify them into a basis of common harmonic wavelets. The performance of our harmonic wavelet analysis has been extensively evaluated in separating clinic cohorts of AD on large-scale neuroimaging data from the ADNI database. Furthermore, we demonstrate the potential application of identifying critical brain regions that are highly relevant to cognitive decline by actively being involved in the spreading of neuropathologies throughout the brain. Our future work includes the understanding of genetic factors in harmonic-based alterations and population stratification based on the harmonic feature representations.

Declaration of Competing Interest

The authors declare that they have no known competing financial interests or personal relationships that could have appeared to influence the work reported in this paper.

Acknowledgments

This work was supported in part by the NIH under Grant AG068399, Grant AG059065, Grant AG049089, and in part by the Alzheimer's Disease Neuroimaging Initiative (ADNI). Jiazhou Chen and Hongming Cai in part supported by the Key-Area Research and Development of Guangdong Province under Grant 2020B1111190001; in part by the National Natural Science Foundation of China under Grant 61771007, Grant 62172112, Grant 62102153, and Grant U21A20520; in part by the Fundamental Research Fund for the Central Universities under Grant x2jsD2200720; in part by the China Postdoctoral Science Foundation under Grant 2021M691062.

Supplementary materials

Supplementary material associated with this article can be found, in the online version, at doi:10.1016/j.media.2022.102446.

References

Aftab, K., et al., 2014. Generalized weiszfeld algorithms for lq optimization. IEEE Trans. Pattern Anal. Mach. Intell. 37, 728–745.
Araque Caballero, M.Á., et al., 2018. White matter diffusion alterations precede symptom onset in autosomal dominant Alzheimer's disease. Brain 141, 3065–3080.
Atasoy, S., et al., 2016. Human brain networks function in connectome-specific harmonic waves. Nat. Commun. 7, 1–10.
Benjamini, Y., Hochberg, Y., 1995. Controlling the false discovery rate: a practical and powerful approach to multiple testing. J. R. Stat. Soc.: Series B (Methodological) 57, 289–300.
Blennow, K., et al., 2006. Alzheimer's disease. Lancet 368, 387–403.
Bloom, G.S., 2014. Amyloid-β and Tau: the Trigger and Bullet in Alzheimer Disease Pathogenesis. JAMA Neurol. 71, 505–508.
Boyd, S., et al., 2011. Distributed Optimization and Statistical Learning Via the Alternating Direction Method of Multipliers. Now Publishers Inc.
Braak, H., Braak, E., 1996. Evolution of the neuropathology of Alzheimer's disease. Acta Neurol. Scand. Suppl. 165, 3–12.
Braak, H., Del Tredici, K., 2018. Spreading of Tau Pathology in Sporadic Alzheimer's Disease Along Cortico-cortical Top-Down Connections. Cereb. Cortex 28, 3372–3384.
Chavel, I., 1984. Eigenvalues in Riemannian geometry. Academic press.
Chen, J., et al., 2020a. Learning Common Harmonic Waves on Stiefel Manifold–A New Mathematical Approach for Brain Network Analyses. IEEE Trans. Med. Imaging 40, 419–430.
Chen, J., et al., 2020b. Estimating Common Harmonic Waves of Brain Networks on Stiefel Manifold. 23rd Internatinal Conference on Medical Image Computing and Computer Assisted Intervention (MICCAI 2020), Lima, Peru.
Chikuse, Y., 2012. Statistics On Special Manifolds. Springer Science & Business Media.
Destrieux, C., et al., 2010. Automatic parcellation of human cortical gyri and sulci using standard anatomical nomenclature. Neuroimage 53, 1–15.
Devanand, D.P., et al., 2010. Pittsburgh compound B (11C-PIB) and fluorodeoxyglucose (18F-FDG) PET in patients with Alzheimer disease, mild cognitive impairment, and healthy controls. J. Geriatr. Psychiatry Neurol. 23.
Filippi, M., et al., 2017. Brain network connectivity differs in early-onset neurodegenerative dementia. Neurology 89, 1764.
Huang, S.G., et al., 2020. Fast Polynomial Approximation of Heat Kernel Convolution on Manifolds and Its Application to Brain Sulcal and Gyral Graph Pattern Analysis. IEEE Trans. Med. Imaging 39, 2201–2212.
Jack, C.R., et al., 2018. NIA-AA Research Framework: toward a biological definition of Alzheimer's disease. Alzheimer's Dementia 14, 535–562.
Kim, W.H., et al., 2015. Multi-resolution statistical analysis of brain connectivity graphs in preclinical Alzheimer's disease. Neuroimage 118, 103–117.
Matthews, P.M., et al., 2012. Brain Structural and Functional Connectivity and the Progression of Neuropathology in Alzheimer's Disease. J. Alzheimers Dis. 33, 163–172.
Mattson, M.P., Magnus, T., 2006. Ageing and neuronal vulnerability. Nat. Rev. Neurosci. 7, 278–294.
Morrison, J.H., Hof, P.R., 1997. Life and death of neurons in the aging brain. Science 278, 412–419.
Palop, J.J., et al., 2006. A network dysfunction perspective on neurodegenerative diseases. Nature 443, 768–773.
Pievani, M., et al., 2014. Brain connectivity in neurodegenerative diseases–from phenotype to proteinopathy. Nat. Rev. Neurol. 10, 620–633.
Raj, A., et al., 2012. A Network Diffusion Model of Disease Progression in Dementia. Neuron 73, 1204–1215.
Raj, A., et al., 2015. Network diffusion model of progression predicts longitudinal patterns of atrophy and metabolism in Alzheimer's disease. Cell Rep. 10, 359–369.
Reisberg, B., et al., 2008. Mild cognitive impairment (MCI): a historical perspective. Int. Psychogeriatr. 20, 18–31.
Saxena, S., Caroni, P., 2011. Selective neuronal vulnerability in neurodegenerative diseases: from stressor thresholds to degeneration. Neuron 71, 35–48.
Schaeffer, E.L., et al., 2011. Insights into Alzheimer disease pathogenesis from studies in transgenic animal models. Clinics 66, 45–54.
Sepulcre, J., et al., 2018. Neurogenetic contributions to amyloid beta and tau spreading in the human cortex. Nat. Med. 24, 1910–1918.
Serran-Pozo, A., et al., 2011. Neuropathological alterations in Alzheimer disease. Cold Spring Harb. Perspect. Med. 1, a006189.
Tan, M., Qiu, A., 2015. Spectral Laplace-Beltrami wavelets with applications in medical images. IEEE Trans. Med. Imaging 34, 1005–1017.
Tombaugh, T.N., McIntyre, N.J., 1992. The mini-mental state examination: a comprehensive review. J. Am. Geriatrics Soc. 40, 922–935.
Vemuri, P., et al., 2009. MRI and CSF biomarkers in normal, MCI, and AD subjects: diagnostic discrimination and cognitive correlations. Neurology 73.
Vogel, J.W., et al., 2020. Spread of pathological tau proteins through communicating neurons in human Alzheimer's disease. Nat. Commun. 11, 2612.
Vogel, J.W., et al., 2021. Four distinct trajectories of tau deposition identified in Alzheimer's disease. Nat. Med. 27, 871–881.
Wang, M., et al., 2016. Integrative network analysis of nineteen brain regions identifies molecular signatures and networks underlying selective regional vulnerability to Alzheimer's disease. Genome Med. 8, 104.
Wu, J.W., et al., 2016. Neuronal activity enhances tau propagation and tau pathology in vivo. Nat. Neurosci. 19, 1085.